Promoted oxygen activation of layered micro-mesoporous structured titanium phosphate nanoplates by coupling nano-sized δ-MnO₂ with surface pits for efficient photocatalytic oxidation of CO

Yanduo Liu[a], Xinjia Zhang[a], Ji Bian[a], Jiawen Sun[a], Zhijun Li[a], Imran Khan[a], Yang Qu[a], Zhibin Li[a,*], Zishi Jiang[b,*], Liqiang Jing[a,*]

[a] Key Laboratory of Functional Inorganic Material Chemistry (Ministry of Education), International Joint Research Center for Catalytic Technology, School of Chemistry and Materials Science, Heilongjiang University, Harbin 150080, PR China
[b] College of Physical Science and Technology, Heilongjiang University, Harbin 150080, PR China

ARTICLE INFO

ABSTRACT

It is highly desired to fabricate efficient micro-mesoporous structured photocatalysts with strong oxygen activation ability for CO oxidation. Herein, a layered micro-mesoporous structured titanium phosphate (L-MMS-TiP) with high photocatalytic activity for CO oxidation has been successfully synthesized by a two-step solvothermal method. The photocatalytic activity of resulting L-MMS-TiP could be greatly improved by coupling a proper amount of nano-sized δ-MnO₂, especially for that with surface pits. The improved activities are mainly attributed to the roles of coupled δ-MnO₂ in enhancing photogenerated charge separation and promoting oxygen activation, which is revealed based on measurements of the steady-state surface photovoltage spectra, nitroblue tetrazolium absorption spectra, electron paramagnetic resonance spectra and in situ DRIFTS spectra. Interestingly, the photocatalytic activity of pitted δ-MnO₂-coupled L-MMS-TiP is superior to that of P25 TiO₂, even much higher than that of Au-coupled L-MMS-TiP. Significantly, δ-MnO₂-coupled L-MMS-TiP also has excellent oxidation removal effect for other harmful or even mixed gases. Moreover, it is confirmed that δ-MnO₂ with the two-dimensional structure is the best one to couple L-MMS-TiP for photocatalytic CO oxidation among all four kinds of crystal phases and compared with other transitional metal oxides. This work opens up a new way to develop a layered micro-mesoporous structure-based nanocomposite, and further improve the photocatalytic activity by promoting oxygen activation with two-dimensional pitted δ-MnO₂.

1. Introduction

With the continuous development of industry and economy, a variety of gaseous pollutants have been inevitably released into the ecosystem, which cause great damage to the human health and environment [1,2]. Carbon monoxide (CO), as a main component of exhaust gas, is toxic, colorless, odorless, tasteless and diffused easily in air. The concentration of CO in the atmosphere is increasing and approaching to the sustainable limit due to the continuous exhaust gas emission from chemical industries and automobile. Therefore, it is highly significant to control CO content in the environment to prevent the long-lasting health hazards caused by CO poisoning mainly through its damaging effects on the central nervous system [3–5]. After years of research, a large number of methods (such as thermocatalysis and electrocatalysis method, etc.) for CO oxidation have emerged [6–8].

However, these techniques are always involved with high energy consumption, easy poisoning and limited application scenarios. Consequently, it is of great significance to develop a without secondary pollution, stable, and multi-application scenarios catalytic technology approach to overcome the above-mentioned drawbacks.

Photocatalytic technology as a promising alternative technique can effectively use solar energy to remove a variety of toxic pollutants, which are difficult to be treated with by traditional processing method [9,10]. Particularly, semiconductor-based photocatalysis has been considered as an inexpensive, renewable, and clean technology, which conducts photocatalytic reactions for a variety of applications. For example, Degussa P25 is widely accepted as the most widespread commercial photocatalyst because of its good photocatalytic activity [11]. However, its practical applications are limited because of the unsatisfactory photoactivities and hard to recycle. The unsatisfactory

---

photoactivities are due to the small specific surface area ($50\,m^2\,g^{-1}$) and non-porous structure, and it is not easy for the small-size (25 nm) nanoparticle powder to be supported and recycled in the case of airflow. Therefore, a kind of photocatalytic material with large BET surface area and increased particle size is highly desirable for an efficient photocatalytic process. In the view of various kinds of materials, porous materials maybe the best choice, due to the specific properties of larger specific surface area, stronger gas adsorption and enrichment capacity, more active sites and better recycling and reuse properties [12]. Especially, the inorganic microporous structured materials have become the most promising photocatalytic material because of their more stable structure, simple preparation process, low cost and the easy availability of raw materials [13]. Thereinto, titanium phosphate with stable thermal stability, suitable band structure, good photocatalytic activity, which should reasonably become a delightful micropores-based material for efficient photocatalysis, unfortunately, it still has received little attention from scientists in the present study [14]. Therefore, it is necessary to take much attention and research on the application of micropores-based titanium phosphate photocatalyst.

Firstly, there is a still one important drawback restricting its application as a high effective photocatalysts, as shown below. The micropores spacing of titanium phosphate is relatively long, which do not have any assistance to the diffusion of the reactants and light, and thus, it is not conducive to the occurrence of the reaction in kinetics terms [15]. Based on the previous works in our group, it is an effective strategy that introducing mesoporous structure into titanium phosphate to form micro-mesoporous structure in order to shorten the transmission distance of the reactants to the desired active sites, and it shows enhanced photocatalytic performance in the oxidation of CO [16]. Therefore, it is highly desirous to synthesize a kind of micro-mesoporous structured titanium phosphate (MMS-TiP) nano-photocatalysts with excellent photoactivity for CO oxidation.

Secondly, to achieve high-efficiency for a photocatalytic reaction, the key is how to effectively use of the photogenerated carriers in a subsequent reaction. However, in combination with the existing literatures, almost all of the prepared titanium phosphates are micronsized bulk, spherical or flower-shaped hierarchically structured materials [17–19]. Although the shape of hierarchically structured material is beautiful and variable, the photogenerated charge transmission distances from the bulk phase to the surface is too long, which increases the probability of photogenerated charge recombination. In this regard, compared with bulk or sphere hierarchically structured structure titanium phosphates, it is extremely important to prepare 2D layered titanium phosphates with extremely short photogenerated carriers transport distance and abundant surface-active sites for promoting the efficient photocatalytic reaction [20]. Thus, it is much feasible to synthesize 2D layered MMS-TiP nanoplate photocatalysts for CO oxidation.

Besides these two problems mentioned above, there is another one important thing need to be conditioned in the designing of photocatalyst which called oxygen activation capacity. Because oxygen as the main reactant in the photocatalytic CO oxidation process, it is more difficult to activate than carbon monoxide as known from experimental analysis and density functional theory calculations [21,22]. As it is known the oxygen activation is carried out by the reduction reaction between photogenerated electrons and oxygen adsorption on the photocatalyst surface, photogenerated electrons lifetime and the oxygen adsorption capacity become the key for oxygen activation. Unluckily, the oxygen activation capacity of titanium phosphate is insufficient. In the light of prolonging photogenerated electrons lifetime problem, coupling a semiconductor material maybe the first choice that can effectively accept photogenerated electrons. Different from 1D or 3D structural materials, semiconductor material with 2D layered structure couples with similar structured titanium phosphate should have better photogenerated charge separation effect. 2D-2D composite could lead to a close contact with a lager contact area due to the dimension matching effect, and the photogenerated charge transport through the interface is smoother and stronger. And now, the last question has to be taken into consideration is oxygen adsorption problem. Various strategies have been studied in order to resolve this shortcoming of titanium phosphate, for example, enhancing the oxygen activation kinetics by modifying precious metals, such as gold, silver and platinum. Yet, precious metals, due to high price, easy to be poisoned and other defects limit their application in practice [23]. Fortunately, some views reported transitional metal oxides with oxygen adsorption and activation function can replace precious metals [24]. On account of these, it is promising to introduce a 2D layered transitional metal oxide with strong oxygen adsorption and activation capacities, so as to achieve effectively solve the bottleneck problem of photocatalytic CO oxidation.

In view of the above-mentioned facts, δ-MnO$_2$ is probably the best choice for coupling with titanium phosphate. Firstly, δ-MnO$_2$ is an infrequent 2D layered transitional metal oxide, so that it is much feasible to maximize the photogenerated charge transfer ability between δ-MnO$_2$ and titanium phosphate due to their dimensional matching [25]. Secondly, according to the studies of Iwamoto and Meng et al., the oxygen adsorption capacity of MnO$_2$ is the highest among these fourth long period transition metal oxides, and large amounts of surface-chemisorbed oxygen species are present on the δ-MnO$_2$ surface, which shows great potential for the activate oxidation used as the cocatalyst [26,27]. Hence, it is a most effective method to improve the photocatalytic performance of 2D layered MMS-TiP nanoplates by coupling δ-MnO$_2$ to enhance photogenerated charge separation and oxygen activation ability.

Many studies have indicated that surface defects, such as step edges, ribs and other low coordination number sites, can provide more active sites and promote the activation reaction [28,29]. For example, Zhang et al. used a nitric acid-treated method to generate much defects (oxygen vacancies and active acidic sites) on the surface of δ-MnO$_2$ for ozone decomposition [30]. Sun et al. reported CeO$_2$ with plentiful surface pits can increase oxygen activation abilities by four- and five-fold [31]. However, in the process of using these means to form surface defects, lack of internal driving force and the difficulty of chemical bond cracking is still a restriction for the effective control of surface structure. As it is known there are a large number of hydrated cations in δ-MnO$_2$ that are used to maintain the charge balance and prevent the structure from collapsing. TBAOH, a macromolecule organic alkali, can smoothly enter into the interlayer of δ-MnO$_2$ to easily replace some hydrated cations, and weaken van der Waals forces to produce much surface pits by steric effect [32]. According to the above analysis, it could be reasonably supposed that the treating of δ-MnO$_2$ by TBAOH can produce many pits, which can effectively promote oxygen activation reaction.

Herein, we have synthesized 2D layered MMS-TiP nanoplates with high photocatalytic CO oxidation activity through a two-step solvothermal method. The photocatalytic activity is further improved by coupling with nano-sized pitted δ-MnO$_2$, which is mainly due to the roles of pitted δ-MnO$_2$ in enhancing photogenerated charge separation and oxygen activation. Noticeably, pitted δ-MnO$_2$-coupled L-MMS-TiP exhibits more excellent photoactivity for CO oxidation performance than commercial P25 TiO$_2$, even much higher than that of Au-coupled L-MMS-TiP. And, for other harmful gases or even mixed ones, it also has superior photocatalytic oxidation effect. Furthermore, among nearly ten alternative materials, 2D structured δ-MnO$_2$ with strong oxygen adsorption and activation abilities is the best one to couple MMS-TiP for photocatalytic CO oxidation. This work opens up a new feasible way to design and synthesize a highly-efficient layered micro-mesoporous structure-based composite to solve CO pollution problem.

2. Experimental

All reagents were analytical grade and were used without further purification, and deionized water was employed throughout.

2.1. Materials synthesis

2.1.1. Synthesis of micro-mesoporous structured titanium phosphate

Bulk micro-mesoporous structured titanium phosphate was synthesized as follows: 1.74 g P123 was dissolved in 20 mL ethanol (ET), and then dropwise added 4 mL acetic acid and 4 mL tetrabutyl titanate (TBT), which was marked as solution A. Subsequently, 6 mL H_3PO_4 solution and 12 mL diluted hydrochloric acid were mixed in 14 mL ET, and then was added into solution A. After stirring for 12 h, the mixture was transferred to a 100 mL Teflon-lined stainless steel autoclave and kept at 180 °C for 12 h. Then the obtained product was washed and dried. Finally, the powder sample was refluxed condensation in 100 mL ET at 80 °C for 24 h for removing template agent. The as-prepared sample is denoted as B-MMS-TiP.

Layered micro-mesoporous structured titanium phosphate was synthesized as follows: 4 mL TBT and 4 mL acetic acid were added dropwise into 20 mL ET to form solution A. Then, 6 mL H_3PO_4 solution and 12 mL diluted hydrochloric acid were mixed in 14 mL ET, and subsequently was added dropwise into solution A. The mixture was transferred to autoclave and heated at 180 °C for 4 h. After the mixture cooled down to room temperature, 1.74 g P123 was added into the mixture. After stirring for 12 h, the mixture was treated at 180 °C for 8 h. The sample was rinsed and dried. The powder sample was refluxed condensation in 100 mL ET at 80 °C for 24 h for removing template agent. The as-prepared sample is denoted as L-MMS-TiP.

2.1.2. Synthesis of δ-MnO₂ coupled L-MMS-TiP

1 g $Mn(NO_3)_2$ was dissolved in 20 mL acetic acid, and kept stirring at 80–90 °C until dryness. The product was annealed at 400 °C for 1 h to form δ-MnO_2. Then, 1 g L-MMS-TiP and a certain amount δ-MnO_2 were dispersed into a mixed solvent of 5 mL distilled water and 20 mL ET. Finally, dried in oven and annealed at a certain temperature for 2 h. The as-prepared samples are denoted as Xδ-MnY/L-MMS-TiP, in which δ-Mn means δ-MnO_2, X represents the mass ratio percentage of used δ-MnO_2 to L-MMS-TiP, and Y is the anneal temperature.

As comparative samples, different raw materials (1 g $KMnO_4$, 0.4 g $MnSO_4$ and 1 g $(NH_4)_2S_2O_8$, 1.8 g $MnSO_4$ and 0.6 g $KMnO_4$, different nitrate compound) were used to couple L-MMS-TiP with the same method as 2δ-Mn400/L-MMS-TiP.

2.1.3. Synthesis of pitted δ-MnO₂ coupled L-MMS-TiP

1 g freshly prepared δ-MnO_2 was dispersed into 100 ml different concentrations (0.1, 0.2 and 0.4 M) TBAOH solution. The mixture was kept under vigorous stirring at 50 °C for 6 h. Then, the sample was rinsed until the pH of the eluate was about 7, and dried at 80 °C for 12 h. Finally, the powder was used to synthesize pitted δ-MnO_2 coupled L-MMS-TiP with the same method as 2δ-Mn400/L-MMS-TiP. The as-prepared samples are denoted as ZH-2δ-Mn400/L-MMS-TiP, in which H stands for TBAOH, and Z is the concentration of TBAOH solution.

A table which contains the raw materials, full name and name abbreviation of different composites is shown in supporting information, as Table S1.

2.2. Characterization techniques

The samples were analyzed by various methods. The X-ray powder diffraction (XRD) was tested with a Bruker D8 Advance diffractometer, using Cu Kα radiation. The UV–vis diffuse reflectance spectrum (DRS) was recorded with a Model Shimadzu UV-2750 spectrophotometer, using $BaSO_4$ as reference. Transmission electron microscopy (TEM) observations were carried out on a JEOL JEM-2010EX instrument operating at a 200 kV accelerating voltage. Scanning electron microscopy (SEM) images were taken using a HitachiS-4800 instrument (Tokyo, Japan), operating at acceleration voltage of 15 kV. Brunauer–Emmett–Teller (BET) surface areas and average pore sizes of samples were determined from N_2 adsorption isotherms at 77 K using

the Quantachrome NOVA2000E specific surface area analyzer after samples had been degassed in the flow of N_2 at 180 °C for 3 h. The steady-state surface photovoltage spectroscopy (SS-SPS) were measured with a self-built equipment, equipped with a lock-in amplifier (SR830, USA) synchronized with a light chopper (SR540, USA). X-ray photoelectron spectroscopy (XPS) using a Kratos-Axis Ultra DLD apparatus with an Al (mono) X-ray source. The electron paramagnetic resonance (EPR) measurements were carried out on a Bruker EMX plus model spectrometer operating at the X-band frequency. The time-resolved surface photovoltage (TR-SPV) measurements were tested by self-built experimental equipment, equipped with a second harmonic Nd: YAG laser (Lab-130-10H, Newport, Co.), high energy pyroelectric sensor (PE50BF-DIF-C, Ophir Photonics Group) and 1GHz digital phosphor oscilloscope (DPO 4104B, Tektronix).

2.3. Evaluation for O₂ temperature programmed desorption

O_2-temperature programmed desorption (O_2-TPD) were performed by Chemisorption Analyzer, TP 5080 Chemisorb with a thermal conductivity detector (TCD). 50 mg sample was preheated at 300 °C for 0.5 h to remove the other adsorbed gases and water and then cooled down to 30 °C under He flow rate of 30 mL min^{-1}. The pure O_2 gas was introduced at 30 °C under O_2 flow rate of 50 mL min^{-1} for 0.5 h. The excess weak physically adsorbed O_2 was removed by He flow rate of 30 mL min^{-1} at 30 °C for 60 min. Then the temperature was increased to 700 °C with the heating rate of 10 °C min^{-1} under He flow rate of 30 mL min^{-1}.

2.4. Photoelectrochemical and hydroxyl radical amount measurements

Photoelectrochemical (PEC) experiment was performed using in a conventional three-electrode electro-chemical quartz cell, filled with 50 mL of 1 M Na_2SO_4 electrolyte. The FTO glass with sample thin film, Pt plate and Ag/AgCl electrode were taken as the working electrode, counter electrode and reference electrode on a LK2006 A workstation, respectively. A 300 W Xenon lamp (wavelength range: 320–780 nm, spot diameter: 60 mm, light power: 134 mW/cm^2) was used as light source.

To measure the hydroxyl radical (•OH) amounts, 0.05 g sample was dispersed in 60 mL of 1×10^{-3} mol L^{-1} aqueous solution in a quartz reactor. At given irradiation time, a certain amount of the solution was transferred into a Pyrex glass cell for the fluorescence measurement of 7-hydroxycoumarin at around 460 nm under the light excitation of 332 nm with a spectrofluorometer (PerkinElmer LS 55).

2.5. In situ DRIFTS measurements

The in situ diffuse reflectance infrared Fourier transform spectroscopy (DRIFTS) analysis was carried out in an in situ diffuse reflectance pool with a Bruker Vector FTIR spectrometer (6700) and MCT detector which was cooled by liquid N_2. Firstly, a certain amount of KBr was filled into the reaction cell, and then covered with 0.2 g catalyst. The reaction cell was placed in the test chamber and heated to 175 °C under N_2 flow for 30 min to remove adsorbed impurities and then cooled to room temperature. In order to simulate the photocatalytic CO oxidation process, the CO (1000 ppm) and O_2 were passed into the reaction cell. In this condition, a certain amount of CO and O_2 could be adsorb on the surface of sample and then purged with N_2. Subsequently, the sample was irradiated under visible light. A 300 W Xenon arc lamp was used as the light source.

2.6. Evaluation of photoactivities

Photocatalytic activities of samples were evaluated by oxidizing CO. A 300 W Xenon arc lamp was used as the light source. 0.1 g sample was put into a 670 mL Pyrex glass cylindrical reactor. A premixed gas
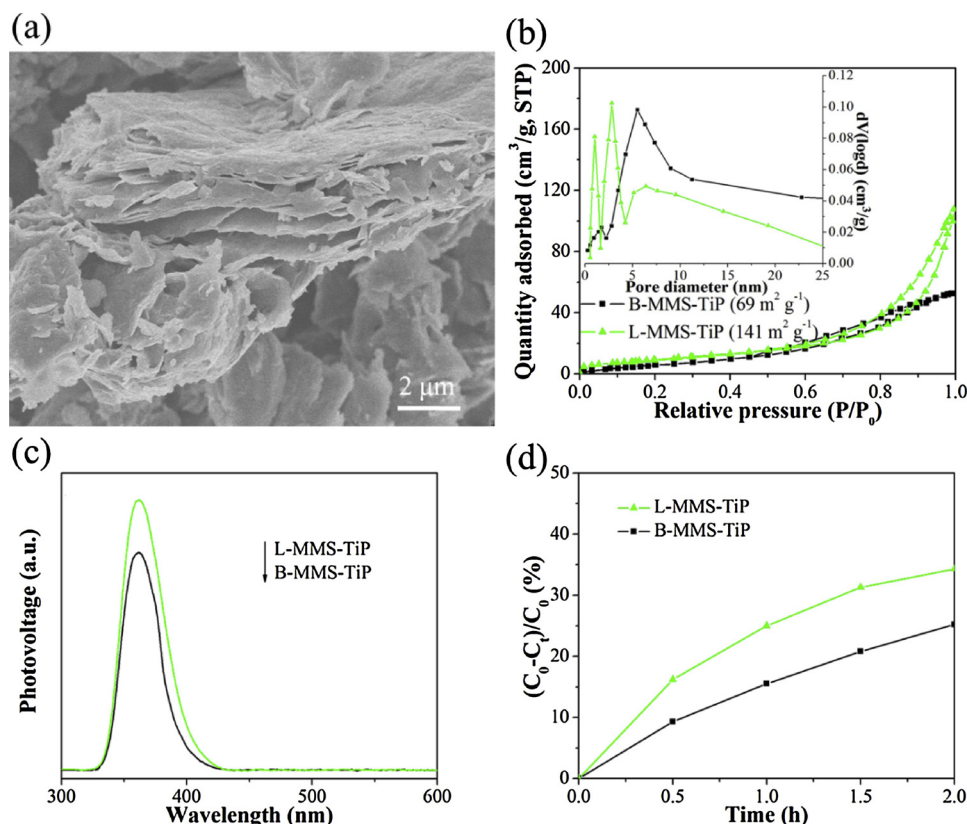
Fig. 1. TEM image of L-MMS-TiP (a), N_2 adsorption–desorption isotherm curves with Pore size distribution Curves in the inset (b), SS-SPS responses (c) and Photocatalytic activities for CO oxidation (d) of different samples.

containing 0.67 mL CO (1000 ppm), 20% O_2, and 80% N_2 was introduced into the reactor. The concentration of CO for every 30 min time interval was measured with a gas chromatograph (GC-7920 with a TCD detector, AuLight, Beijing). In addition, the photocatalytic activities of acetaldehyde and mixed gas (acetaldehyde and CO) were carried out in the same manner.

3. Results and discussion

3.1. Effects of layered structure

The XRD patterns of resulting samples are presented in Fig. S1a, one can notice that typical diffraction peaks are associated with the α-titanium phosphate (JCPDS No. 83-0109). What is noteworthy is that the L-MMS-TiP displays a new characteristic peak at 8.8°, which characteristically corresponds to the layered structure [19]. This result implies that the layered MMS-TiP has been successfully synthesized. The DRS spectra (Fig. S1b) indicate the band absorption edge of samples appears at 356 nm, which is consistent with the literature [33]. Microscopic morphologies of MMS-TiP samples are shown by SEM images (Fig. 1a, Fig. S2) and TEM images (Fig. S3). It has been proved that the layered structure does not change the crystal phase structure of MMS-TiP by XRD patterns. Thus, one can see from EDX spectrum that the atomic percentage composition of L-MMS-TiP is basically the same as that of B-MMS-TiP, similar to the theoretical value.

Different from B-MMS-TiP, it is clearly demonstrated that the morphology of L-MMS-TiP is uniform nanoplates. As revealed in the zoomed area (Fig. S3b), there are rather densely packed micro-mesoporous structures. These results indicate that the layered structure does not change the crystal phase composition and optical absorption characteristics of MMS-TiP.

The N_2 sorption isotherm curves and pore size distribution curves of samples are shown in Fig. 1b. It is easy to see there are characteristic type I and type IV shapes for samples, attributed to the micro-mesoporous structure. Comparably, L-MMS-TiP exhibits the largest hysteresis loop, which indicates the best micro-mesoporous structure. It clearly illustrates the BET surface area and the external surface areas have been increased due to the more micro-mesoporous structure as shown in Table S2. The B-MMS-TiP shows a broad mesoporous size distribution in the range of 3–20 nm, while L-MMS-TiP shows few mesoporous pore size ranges, with the more concentration in the range of 3 nm, which is consistent with the TEM results. This can be explained as that the layered structure is more conducive to increase the specific surface area.

The SS-SPS is a direct and valid mean to investigate the nature of photogenerated charges in a semiconductor. In general, the stronger SS-SPS response, the higher photogenerated charge separation. As shown in (Fig. 1c), it is clear that the SS-SPS response of L-MMS-TiP is significantly enhanced, implying the better photogenerated charge separation. The produced •OH amount (Fig. S4) indirectly reflects the photogenerated charge separation. Obviously, the fluorescence spectra result is in good agreement with the above SS-SPS one. This further proves that the layered structure is favorable for the charge separation enhancement.

Based on the above analyses, it is naturally expected that L-MMS-TiP is in favor of photocatalytic CO oxidation. As shown in Fig. 1d, compared with B-MMS-TiP (24%), it is clear that L-MMS-TiP (35%) possesses the much better CO oxidation performance. This is largely due to the layered micro-mesoporous structure not only providing larger specific surface areas to favor light harvesting and to increase surface accessibility to reactants, but also shortening the transfer distance of photogenerated charge and inhibiting the photogenerated charge recombination.
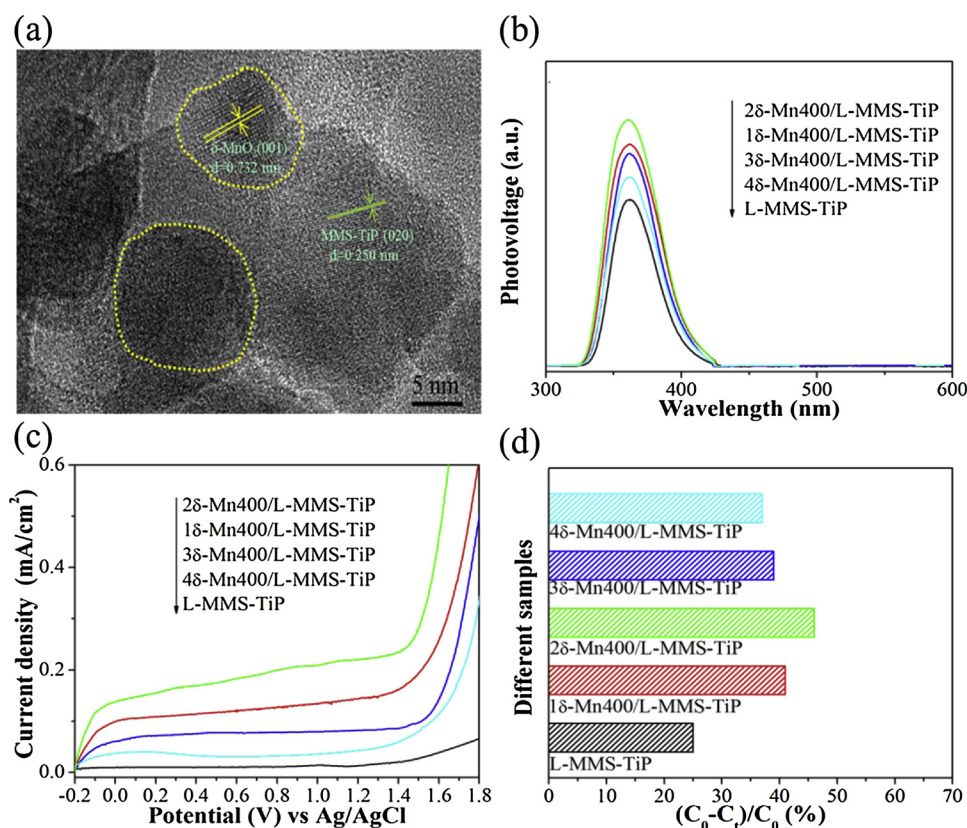
Fig. 2. HRTEM image of 2δ-Mn400/L-MMS-TiP (a), SS-SPS responses (b), I–V curves under irradiation with UV–Vis light (c) and Photocatalytic activitives for CO oxidation (d) of different samples.

3.2. Effects of coupling δ-MnO₂

δ-MnO₂/L-MMS-TiP composites show nearly the same properties as the L-MMS-TiP in crystal phase, optical absorption and surface textures as shown in Figs. S5, 6 and 7. The morphology of 2δ-Mn400/L-MMS-TiP was shown by HRTEM images (Fig. 2a) and SAED pattern (Fig. S8). It indicates that the nano-sized δ-MnO₂ with average 15 nm in diameter is well distributed on the L-MMS-TiP surface. Moreover, a compact interface between L-MMS-TiP and δ-MnO₂ can be observed, since the lattice spacing values are 0.250 and 0.732 nm, respectively matching well with the planes of L-MMS-TiP (020) and δ-MnO₂ (001), and are well dispersed according to Fig. S8. [16,34,35]. These results indicate that a 2D-2D nanocomposite with dimension matching is formed without changing the crystal phase, optical absorption and surface textures.

Photophysical and photoelectrochemical methods were carried out to inquire into the photogenerated charge separation and transfer. As shown in Fig. 2b and Fig. S9a, L-MMS-TiP has a weak signal at ˜360 nm, which can be ascribed to the weak separation of photogenerated charge. Noticeably, the SS-SPS intensity of L-MMS-TiP is significantly increased after coupling δ-MnO₂, and the 2δ-Mn400/L-MMS-TiP sample exhibits the strongest SS-SPS response, indicating the most outstanding photogenerated charge separation. It is further supported by the enhanced amount of produced •OH by FS analyses (Fig. S10a and b).

The PEC performance of the composites was inquired to further verify the effect of coupled δ-MnO₂. As shown in Fig. 2c and Fig. S9b, for L-MMS-TiP, the photocurrent density increases slowly compared with the composites, and the difference becomes more obvious when the applied voltage increases. As shown in the results, 2δ-Mn400/L-MMS-TiP photocurrent density at 0.4 $V_{Ag/AgCl}$ is ˜15 times higher than that of L-MMS-TiP. Moreover, the onset potential of 2δ-Mn400/L-MMS-TiP shifts negatively, which reduces the driving external force of PEC

process. Therefore, it is can be concluded that the δ-MnO₂ would play an important role in enhancing the photogenerated charge separation. Additionally, the photocurrent density-time (I − t) curves (Fig. S10c and d) were plotted at 0.4 $V_{Ag/AgCl}$ attest that the photocurrent is highly repeatable with the cycle of turning on/off the light. After nearly 1000s, the photoelectric current densities of all samples do not significantly decrease, indicating that composites have good photoelectrochemical stability.

The photoactivities for CO oxidation of different samples are shown in Fig. 2d and Fig. S9c. It is clearly seen that the photoactivity could be improved after coupling δ-MnO₂. In particular, 2δ-Mn400/L-MMS-TiP exhibits the best photoactivity with a 20% oxidation rate enhancement compared with L-MMS-TiP.

Since coupling with δ-MnO₂ could enhance the photogenerated charge separation and improve the photoactivity of L-MMS-TiP. To verify the effects of other crystalline phases MnO₂ and different transitional metal oxides, we have also synthesized other nearly ten kinds of composites. It can be seen that the crystal phase, crystallinity and optical absorption characteristic of all composites nearly keep unchanged after coupling with other materials (Figs. S11 and 12).

Compared to L-MMS-TiP, the composites exhibit higher photogenerated charge separation, in which 2δ-Mn400/L-MMS-TiP exhibits the highest one, based on the observed SS-SPS responses and the produced •OH amount analyses (Figs. S13 and S14). As expected, among the resulting composites, 2δ-Mn400/L-MMS-TiP displays the highest photoactivity for CO oxidation (Figs. S15 and S16). This is mainly because δ-MnO₂ is the sole 2D layered structure among these crystalline phases MnO₂. Due to the dimension matching effect, 2D-2D composite could lead to a close contact with a lager contact area, so that the photogenerated charge separation through the interface could be smoother and stronger. In addition, among transition metal oxides, it can be found that O₂ adsorption capacity of δ-MnO₂ is the strongest one (Fig. S17). O₂ is the main receptor of photogenerated electrons and

reactant in the photocatalytic CO oxidation process, the increase of O_2 adsorption capacity could greatly promote photogenerated charge separation and improve the O_2 activation kinetics. The above two points explain why 2δ-Mn400/L-MMS-TiP can exhibit the best photogenerated charge separation and photoactivity for CO oxidation.

3.3. Effects of coupling pitted δ-MnO₂

In order to further promote the photogenerated charge separation, O_2 adsorption and activation abilities of resulting composites, Tetrabutylammonium Hydroxide (TBAOH) was used to synthesize pitted δ-MnO₂. It can be clearly seen that the crystal phase and optical properties of 2δ-Mn400/L-MMS-TiP are not affected (Fig. S18). XPS spectra were surveyed to further investigate the chemical configurations and the interfacial interactions between L-MMS-TiP and δ-MnO₂/ pitted δ-MnO₂. As shown in Ti 2p and P 2p spectra (Fig. S19a and b), one can notice that the binding energies of Ti 2p and P 2p of the resulting composite are higher than those of L-MMS-TiP [36]. This is mainly due to the electron transfer from L-MMS-TiP to δ-MnO₂ after L-MMS-TiP bonded with δ-MnO₂, which reduces the density of outer electron cloud of Ti and P. This also proves that δ-MnO₂ is successfully coupled on the surface of L-MMS-TiP. Fig. S19c presents the O 1s broad peaks with asymmetric feature, which are deconvolved into two peaks around 530.0 eV (crystal lattice oxygen, O_L) and 531.0–532.0 eV (surface adsorption oxygen, O_H). The O_L binding energy of L-MMS-TiP shifts from 530.0 to 530.3 eV for 2δ-Mn400/L-MMS-TiP, indicating that the presence of δ-MnO₂ causes a stronger interaction. In addition, the $O_H/(O_L + O_H)$ molar ratio is calculated. Compared with that of L-MMS-TiP (30.0%), the value of 0.2H-2δ-Mn400/L-MMS-TiP could reach 41.7%, which is due to the presence of oxygen vacancy. At the same time, abundant oxygen vacancies also indicate that the sample may have excellent oxygen adsorption ability, which is further proved by the following O_2-TPD experiment result. The Mn 2p core level spectra

(Fig. 3a) show two obvious peaks of the characteristic spin–orbit splitting of Mn $2p_{3/2}$ and Mn $2p_{1/2}$, which demonstrates the existence of MnO₂.

Compared with pure δ-MnO₂ (641.8 eV), the Mn $2p_{3/2}$ binding energy of 2δ-Mn400/L-MMS-TiP is lower [35]. This could be explained that δ-MnO₂ receives electrons from L-MMS-TiP, and thus increases the electron density of Mn 2p. This is consistent with the above change of Ti 2p and P 2p spectra. The binding energy of Mn $2p_{3/2}$ located at 641.4 eV for 2δ-Mn400/L-MMS-TiP is shifted to 640.7 eV for 0.2H-2δ-Mn400/L-MMS-TiP, which indicates that part of Mn^{4+} has been converted to Mn^{3+}. It can be understood that many oxygen vacancies exist in the surface pits, resulting in the increased electron density around Mn^{4+}, thus promoting the conversion of Mn^{4+} to Mn^{3+}. Based on the XPS results, it is deduced that the pitted δ-MnO₂ is successfully coupled on the L-MMS-TiP surface.

The photogenerated charge separation of resulting composites is evaluated from the three aspects of photophysics, photochemistry and photoelectrochemistry (Fig. 3b, c and Fig. S20). Unsurprisingly, after coupling pitted δ-MnO₂, the SS-SPS signal, produced •OH amount and photocurrent density of the composites are greatly improved. All of the outcomes represent that pitted δ-MnO₂ has a better effect on promoting L-MMS-TiP photogenerated charge separation.

Since Au is the most effective catalyst in CO oxidation process, and commercial P25 TiO₂ is the well-recognized standard photocatalyst. Therefore, taking their practical applications into consideration, the photoactivities of representative samples for oxidizing CO have been investigated, especially in comparison to 2Au/L-MMS-TiP and P25 TiO₂ (Fig. 3d). It is gratifying that the 0.2H-2δ-Mn400/L-MMS-TiP (~ 60%) is superior to P25 (~ 40%) and 2Au/L-MMS-TiP (~ 55%) in photoactivity. Moreover, in order to further explain the best photocatalyst activity, the TOF values as a function of α-titanium phosphate have been calculated and compared for different samples. The TOF values of L-MMS-TiP, 2δ-Mn400/L-MMS-TiP and 0.2H-2δ-Mn400/L-MMS-TiP are 0.019, 0.036
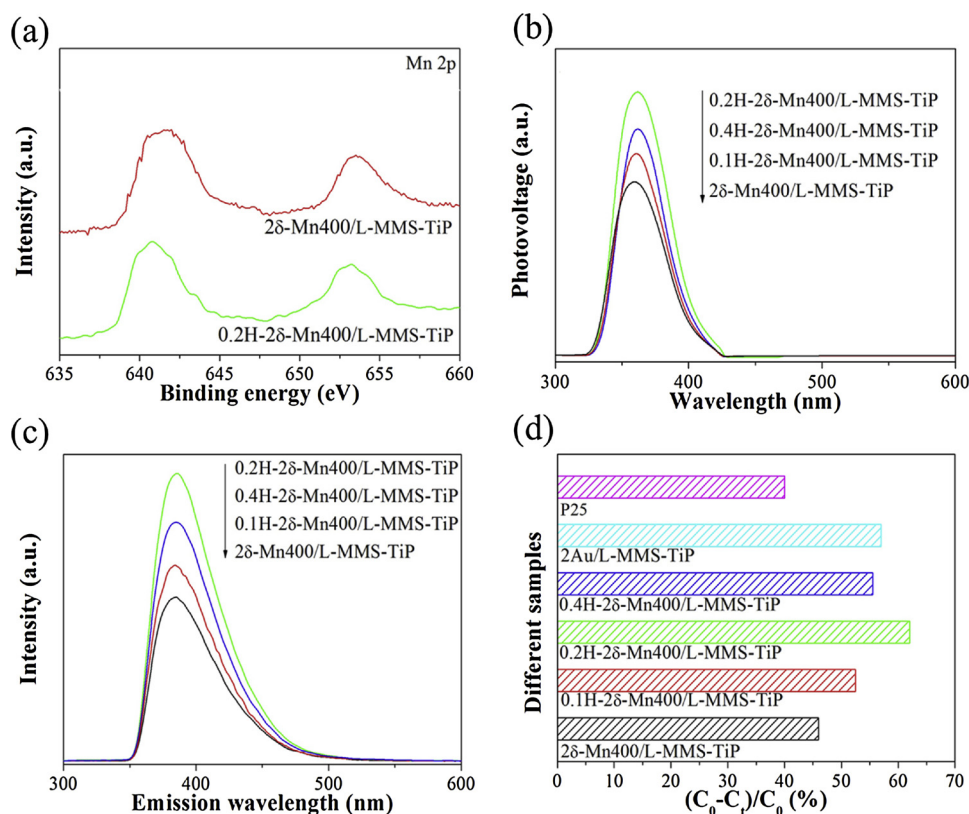

Fig. 3. XPS spectra of Mn 2p (a), SS-SPS responses (b), Fluorescence spectra related to the amounts of hydroxyl radical formed after irradiation for 1 h (c) and Photocatalytic activitives for CO oxidation (d) of different samples.

and 0.049 h^{-1}, respectively (the calculation method is listed in the support information). This is attributed to the fact that the pitted δ-MnO$_2$ can adsorb more oxygen, provide more receptors for photo-generated electrons and achieve effective O$_2$ activation. The stability of 0.2H-2δ-Mn400/L-MMS-TiP was also measured, as shown in Fig. S21. It shows that the photoactivity of the 0.2H-2δ-Mn400/L-MMS-TiP is nearly not changed after five cycles, indicating that the pitted δ-MnO$_2$-coupled L-MMS-TiP is stable.

To further support the above result, we have measured the oxidation activity of acetaldehyde of resulting composites, also with 2Au/L-MMS-TiP as the comparative sample (Figs. S22a and S23a), it is clearly found that 0.2H-2δ-Mn400/L-MMS-TiP exhibits the best photocatalytic performance. In addition, CO rarely exists as a single pollution source in daily life, and often coexists with other volatile gases. In view of this, mixed gas (acetaldehyde and CO) oxidation removal test was also performed on representative samples and 2Au/L-MMS-TiP (Figs. S22b and S23b). It is not hard to see that 0.2H-2δ-Mn400/L-MMS-TiP also shows the best better oxidation performance for the mixed gas. These results demonstrate that 0.2H-2δ-Mn400/L-MMS-TiP possesses good universal applicability.

3.4. Discussion

The photogenerated charge separation mechanism was investigated by the atmosphere-controlled SS-SPS spectra (Fig. 4a), TR-SPV responses (Fig. 4b) and Nyquist plots for electrochemical impedance spectra (Fig. S24). It is clear that the pure L-MMS-TiP shows no SS-SPS response in N$_2$, while the SS-SPS response obviously increases after coupling δ-MnO$_2$, especially for the coupled pitted δ-MnO$_2$. Notably, the SS-SPS responses of 0.2H-2δ-Mn400/L-MMS-TiP in air and O$_2$ are much significant. Subsequently, the photogenerated charge separation dynamics were also investigated by TR-SPV responses (Fig. 4b). The pure L-MMS-TiP shows a positive TR-SPV signal under laser pulse illumination, which means that the photogenerated electrons are effectively captured and the photogenerated holes are accumulated on the surface of the composite. It is noticed that the 0.2H-2δ-Mn400/L-MMS-TiP sample exhibits the largest positive TR-SPV response intensity with an obvious ~ ms extension. Besides, the Nyquist plots for electrochemical impedance spectra (Fig. S24) were enforced to reflect the interfacial photogenerated charge transfer effects. The radius of EIS advises a photogenerated charge transfer resistance at the interface (R$_{CT}$). The smallest R$_{CT}$ of 0.2H-2δ-Mn400/L-MMS-TiP implies the lowest photogenerated charge transfer resistance, the highest electro-conductibility, and the fastest transportation of photogenerated charges, which are completely consistent with the above SS-SPS and TR-SPV results on the greatly-enhanced charge separation. Based on our previous works, it is expected that the adsorbed oxygen is an acceptor for the photogenerated electron. Thus, the obviously-enhanced photo-generated charge separation and the prolonged photogenerated charge lifetime are close related to the promoted adsorption of O$_2$ on resulting nanocomposites. Briefly, the more is the adsorbed oxygen, the better is the photogenerated charge separation.

Subsequently, the electrochemical reduction experiments with the O$_2$-bubbled system of different samples were measured to obtain a deep insight into the uncommon photoactivities for CO oxidation mechanism, as shown in Fig. 4c and S25. It is noticed that the potential on δ-MnO$_2$/L-MMS-TiP electrode, especially on pitted δ-MnO$_2$/L-MMS-TiP, for O$_2$ activation shift to the low value compared to that on L-MMS-TiP. This demonstrates that it is obviously favored thermodynamically to activate O$_2$ on 0.2H-2δ-Mn400/L-MMS-TiP. Thus, it is deduced that the adsorbed O$_2$ would effectively capture photogenerated electrons to promote O$_2$ activation and produce •O$_2^-$, which is consistent with the previous conjecture. Further survey was carried out to investigate the O$_2$ activation and radical generation mechanism in the in-depth reaction process by EPR detection at room temperature (Fig. 4d). Compared with pure L-MMS-TiP and 2δ-Mn400/L-MMS-TiP, 0.2H-2δ-Mn400/L-

MMS-TiP possesses an obvious EPR peak with a g-tensor of 2.001, which is ascribed to the inherent oxygen vacancy of pitted δ-MnO$_2$ [37]. It can be seen that all samples in O$_2$ atmosphere lead to the formation of another typical signal at g = 2.005 under light irradiation, corresponding to the produced •O$_2^-$. Meanwhile, 0.2H-2δ-Mn400/L-MMS-TiP has the strongest •O$_2^-$ EPR signal, indicating the strongest photogenerated electron-hole pair separation and O$_2$ activation ability. In addition, the generation of reactive oxygen species over the representative composites was probed by a DMPO spin-trapping EPR technique. A four-line EPR signal with an intensity ratio of 1:1:1:1 is observed under UV–vis light irradiation, which is characteristic of DMPO-•O$_2^-$ adducts (Fig. 4e) [38]. Thus, it can be concluded that the photogenerated electrons are easily captured by the adsorbed O$_2$ to produce •O$_2^-$ on L-MMS-TiP based photocatalyst. In particular, after introducing δ-MnO$_2$, there is a significant increase in the •O$_2^-$ EPR signal, especially for the 0.2H-2δ-Mn400/L-MMS-TiP. This indicates that the surface pits would provide more adsorption and active sites for O$_2$. Finally, nitroblue tetrazolium (NBT) transformation mean was used to further explore the O$_2$ activation behavior. The relatively generated amount of •O$_2^-$ in the O$_2$ activation process is calculated by the absorbance of NBT at 260 nm. As shown in Fig. 4f, the decrease rate of NBT absorbance is the fastest on 0.2H-2δ-Mn400/L-MMS-TiP with increasing the illumination time, confirming that 0.2H-2δ-Mn400/L-MMS-TiP possesses the strongest O$_2$ activation ability. Similar to the photogenerated charge separation, the strong oxygen activation ability is also assigned to the adsorbed O$_2$ on the surface of the sample. Generally, the more is the adsorbed O$_2$ on the photocatalyst, the easier is the O$_2$ activation.

In view of the fact that the photogenerated charge separation mechanism and the oxygen activation mechanism are related to the O$_2$ adsorption capacity, the O$_2$-TPD analyses (Fig. 5a and Fig. S26) were used to study the deep reasons for photogenerated charge separation and O$_2$ activation on photocatalysts. It can be seen the O$_2$ adsorption capacity of L-MMS-TiP increases significantly after coupling δ-MnO$_2$. Careful observation reveals that the chemisorbed O$_2$ desorption peaks (above 300 °C) of all δ-MnO$_2$/L-MMS-TiP samples move to a higher temperature, indicating that the ability to bond with O$_2$ is enhanced after coupling δ-MnO$_2$. The same situation also occurs in the pitted δ-MnO$_2$/L-MMS-TiP samples, which indicates that the pitted δ-MnO$_2$ possess a stronger adsorption O$_2$ ability. As a result, the promoted O$_2$ adsorption greatly facilitates the photogenerated charge separation and O$_2$ activation.

As fully explained above about the photoactivity for CO oxidation improvement mechanism of resulting composite photocatalyst, the reaction mechanism of CO oxidation was also well investigated. It can be seen from the CO-O$_2$ mixed gas TPD analyses (Fig. S27), the CO desorption curves of all samples are basically unchanged, indicating that the adsorption sites for CO mainly come from L-MMS-TiP. As for the mixed gas cases (Fig. 5b), the mixed gas adsorption behavior of the samples are highly similar to the O$_2$-TPD ones, indicating that the O$_2$ adsorption capacity in this system is dominant compared with that of CO. This also shows that the enhancement of photocatalytic performance is mainly dependent on the O$_2$ adsorption and activation.

In light of the fact that the CO oxidation reaction is performed in a closed environment, it is possible that a large amount of generated CO$_2$ may adsorb on the reactive sites so as to inhibit the reaction ahead. For this, a deliberately designed experiment was carried out for 0.2H-2δ-Mn400/L-MMS-TiP: CO$_2$ is firstly adsorbed on the sample, and then to adsorb O$_2$. After that, subsequent desorption is conducted. As shown in Fig. 5c, in the presence of CO$_2$, the O$_2$ desorption peak intensity of L-MMS-TiP significantly decreases, indicating that the O$_2$ adsorption sites are easily occupied by pre-adsorbed CO$_2$. Different from L-MMS-TiP, there is no significant change in O$_2$ desorption peak of 0.2H-2δ-Mn400/L-MMS-TiP, no matter whether CO$_2$ is pre-adsorbed or not, meaning that the pitted δ-MnO$_2$ has a strong O$_2$ selective adsorption capacity.

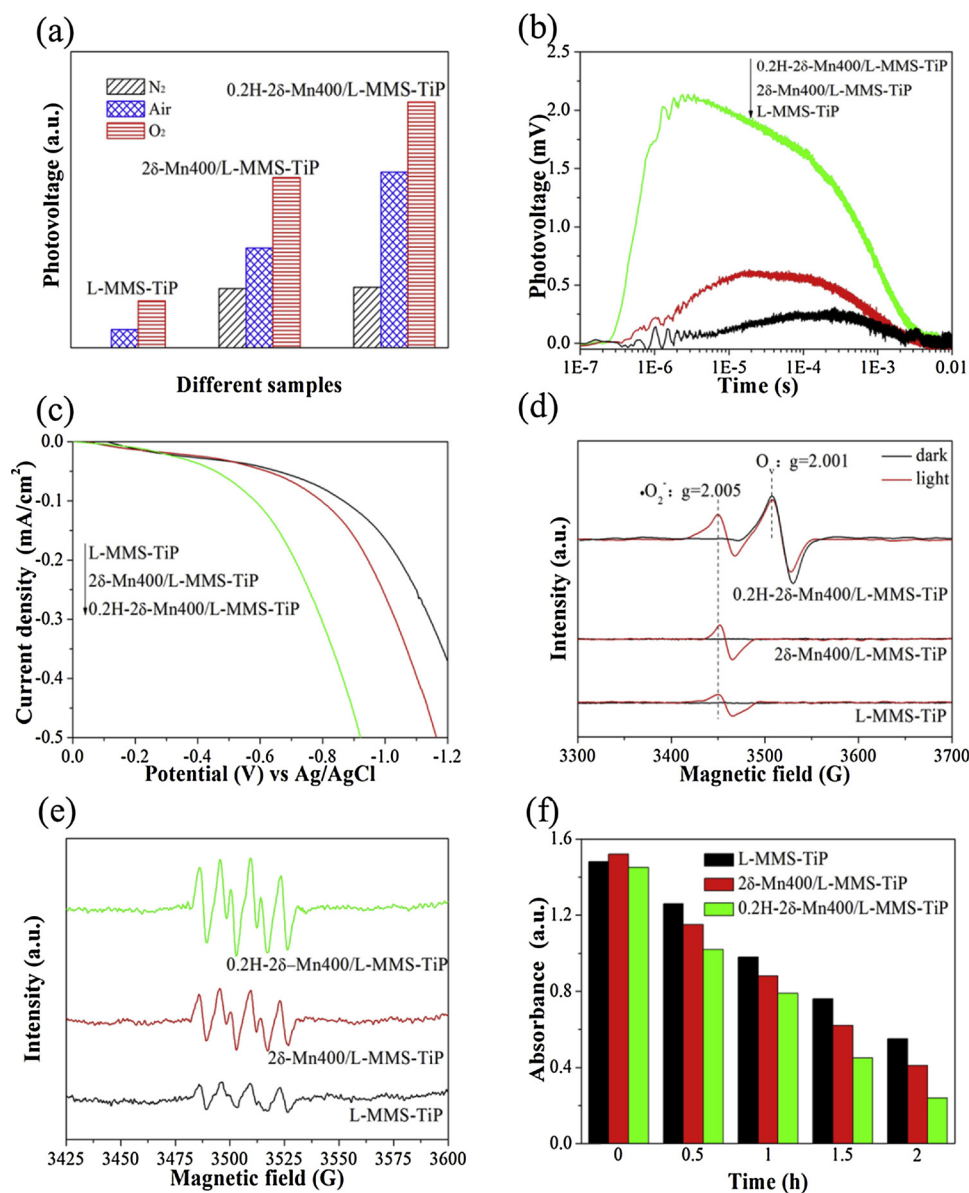Combining with various gas-TPD analyses, a comprehensive in-situ

Fig. 4. Intensities of SS-SPS response peak at 354 nm in different atmospheres (a), TR-SPV responses (b), Electrochemical reduction curves in the O_2-bubbled (c), EPR spectra under different conditions (d), EPR spectra of the DMPO-$\cdot O_2{}^-$ adducts recorded under UV–vis light irradiation (e) and Absorbance of nitroblue tetrazolium at 260 nm under light irradiation (f) of different samples.

DRIFTS analysis on that the pre-adsorbed CO reacts with O_2 on the representative samples under light irradiation has been given in Fig. 5d. When the samples are firstly exposed to 1000 ppm CO and then purged by O_2 (20%) + N_2, which is remarked as 0 min, there is only CO adsorption peak observed at 2000 cm^{-1}. When the samples were exposed to the light, the band at 2000 cm^{-1} declines significantly, while the band at 2300 cm^{-1} assigned to CO_2 increases gradually [39]. This indicates that the CO pre-adsorbed on the samples could react quickly with O_2 to form CO_2 after light illumination. These processes are more pronounced on 2δ-Mn400/L-MMS-TiP. Interesting changes have taken place on $0.2H$-2δ-Mn400/L-MMS-TiP sample, the band of CO disappears completely after 15 min of light, and then the band of CO_2 also drops and even disappears after 20 min of light. This clearly shows that the $0.2H$-2δ-Mn400/L-MMS-TiP not only exhibits better photocatalytic performance, but also better desorption capacity of CO_2. This is exactly consistent with the above TPD results, proving that the improved photocatalytic CO oxidation activity of $0.2H$-2δ-Mn400/L-MMS-TiP mainly depends on the pitted δ-MnO$_2$ with strong O_2 adsorption ability and weak CO_2 desorption capacity.

Based on the above discussion, a possible photocatalytic CO oxidation process mechanism on the pitted δ-MnO$_2$ coupled L-MMS-TiP composite sample is illustrated in Fig. 6. With respect to CO oxidation, under the UV–vis light irradiation, the photogenerated electrons in the VB (3.0 eV) of L-MMS-TiP can be excited to the CB (-0.5 eV), and then transfer to the CB (-0.17 eV) of pitted δ-MnO$_2$ [16,40]. The empty 3d orbit of Mn^{4+} can combine with lone pair electrons of O_2, and the oxygen defects of pitted δ-MnO$_2$ can capture more O_2, thus adsorbing a large amount of O_2 by synergistic effect. Thus, the large amounts of adsorbed O_2 on the pitted δ-MnO$_2$ surface are liable to be activated by the photogenerated electrons to form $\cdot O_2{}^-$. Meantime, CO is activated by h$^+$ to form CO$^+$. Due to the spillover effect, $\cdot O_2{}^-$ reacts with CO$^+$ to form CO_2 [41–43].

The photoactivity for oxidation CO of as-synthesized pitted δ-MnO$_2$/L-MMS-TiP composite is quite impressive compared with other photocatalysts [44–48]. The selected results in CO removal on some reported photocatalysts including our previous work are listed in Table S3. Therefore, this work has important reference value for improving the performance of photocatalytic CO oxidation.
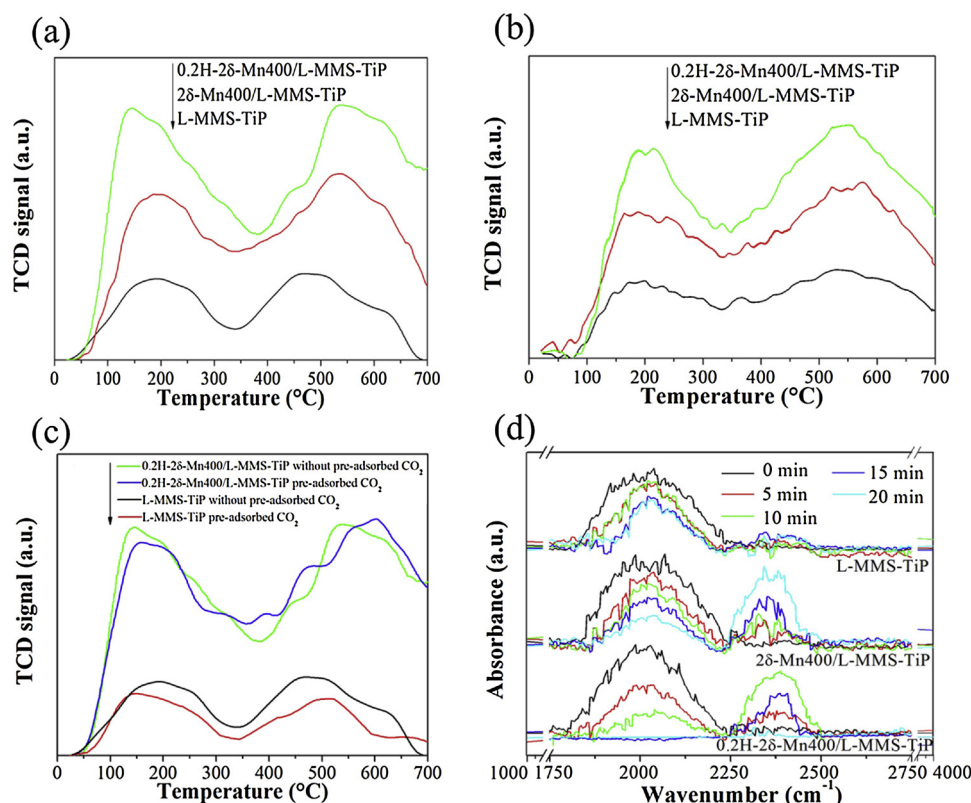
Fig. 5. O_2 temperature-programmed desorption curves (a), Mixed gas of CO and O_2 temperature-programmed desorption curves (b), Mixed gas of CO_2 and O_2 temperature-programmed desorption curves (c) and In situ DRIFTS spectra at room temperature (d) of different samples.
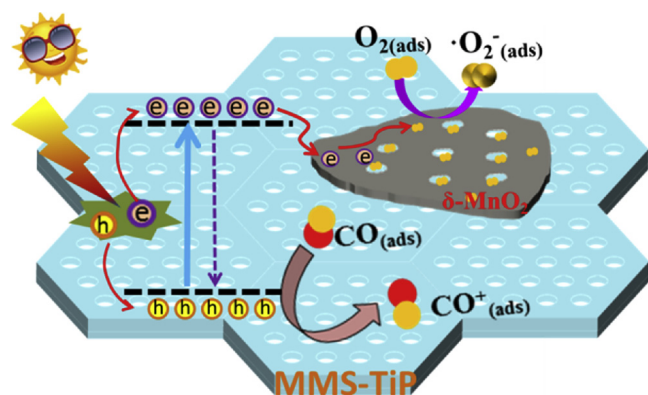

Fig. 6. Schematic of the photogenerated charge transfer and separation, and the UV–vis light induced photocatalytic CO oxidation processes on 0.2H-2δ-Mn400/L-MMS-TiP nanocomposite.

4. Conclusions

In summary, the pitted δ-MnO_2/L-MMS-TiP with strong O_2 activation ability has been successfully synthesized via an easy wet-chemical method, as an efficient nano-photocatalyst for CO oxidation. It is clearly shown that the resulting pitted δ-MnO_2/L-MMS-TiP exhibits excellent photocatalytic performance, which is superior to that of P25 TiO_2, even much higher than that of Au coupled L-MMS-TiP. Significantly, this resulting sample also has prominent oxidation removal effect for other harmful or even mixed gases. The superior photoactivities should be given the credit to the large surface area and the beneficial charge separation of the resulting L-MMS-TiP, and the enhanced charge separation and the promoted O_2 activation of coupled pitted δ-MnO_2. Moreover, compared with other transitional metal oxides and among four kinds of MnO_2 crystal phases, it is confirmed that δ-MnO_2 with the

two-dimensional structure is the best one to couple MMS-TiP for photocatalytic CO oxidation. This work opens up a new way to design and preparation of highly efficient layered micro-mesoporous structure titanium phosphate-based photocatalysts for removing CO.

Acknowledgements

Appendix A. Supplementary data

Supplementary material related to this article can be found, in the online version, at doi:https://doi.org/10.1016/j.apcatb.2019.05.004.

References

[1] M. Shikhar, L.G. Li, D. Zhang, J. Jian, Z.M. Qi, M. Fan, H.T. Chen, X.H. Zhang, H.Y. Wang, Self-assembled ordered three-phase Au-BaTiO$_3$-ZnO vertically aligned nanocomposites achieved by a templating method, Adv. Mater. 31 (2018) 1806529.

[2] A. Zada, M. Humayun, F. Raziq, X.L. Zhang, Y. Qu, L.L. Bai, C.L. Qin, L.Q. Jing, H.G. Fu, Exceptional visible-light-driven cocatalyst-free photocatalytic activity of g-C$_3$N$_4$ by well-designed nanocomposites with plasmonic Au and SnO$_2$, Adv. Energy Mater. 6 (2016) 1601190.

[3] M.Z. Xie, X.D. Fu, L.Q. Jing, P. Luan, Y.J. Feng, H.G. Fu, Long-lived, visible-light-excited charge carriers of TiO$_2$/BiVO$_4$ nanocomposites and their unexpected photoactivity for water splitting, Adv. Energy Mater. 4 (2014) 1300995.

[4] K. Zhang, L.F. Li, S. Shamil, F. Hans-Joachim, Carbon monoxide oxidation on metal-supported monolayer oxide films: establishing which interface is active, Angew. Chem. Int. Ed. 57 (2018) 1261–1265.

[5] W. Li, X.L. Feng, Z. Zhang, X. Jin, D.P. Liu, Y. Zhang, A controllable surface etching strategy for well-defined spiny yolk@shell CuO@CeO$_2$ cubes and their catalytic performance boost, Adv. Funct. Mater. 28 (2018) 1802559.

[6] X. Zhou, Q. Shen, K.D. Yuan, W.S. Yang, Q.Y. Chen, Z.H. Geng, J.L. Zhang, X. Shao, W. Chen, G.Q. Xu, X.M. Yang, K. Wu, Unraveling charge state of supported Au single-atoms during CO oxidation, J. Am. Chem. Soc. 140 (2018) 554–557.

[7] J.X. Liu, Y.Q. Su, A.W.F. Ivo, J.M.H. Emiel, A linear scaling relation for CO oxidation on CeO_2-supported Pd, J. Am. Chem. Soc. 140 (2018) 4580–4587.

[8] L. Shang, Y.H. Liang, M.Z. Li, I.N.W. Geoffrey, P. Tang, D. Ma, L.Z. Wu, C.H. Tung, T.R. Zhang, "Naked" magnetically recyclable mesoporous Au-γ-Fe_2O_3 nanocrystal clusters: a highly integrated catalyst system, Adv. Funct. Mater. 27 (2017) 1606215.

[9] X.L. Hu, H. Zhao, J. Tian, J.X. Gao, Y.Y. Li, H.Z. Cui, Synthesis of few-layer MoS_2 nanosheets-coated TiO_2 nanosheets on graphite fibers for enhanced photocatalytic properties, Sol. Energy Mater. Sol. Cells 172 (2017) 108–116.

[10] M. Rakibuddin, R, Ananthakrishnan. Fabrication of graphene aerosol hybridized coordination polymer derived $CdO/SnO2$ heteronanostructure with improved visible light photocatalytic performance, Sol. Energy Mater. Sol. Cells 162 (2017) 62–71.

[11] E.K. Roghi, Y. Sudheera, A. Aria, P.T. Carl, P25 titanium dioxide coated magnetic particles: preparation,characterization and photocatalytic activity, Appl Catal B-Environ. 187 (2016) 249–258.

[12] Y. Hiromi, M. Kohsuke, K. Yasutaka, K. Takashi, M.C. Wen, V. Priyanka, C. Michel, Single-site and nano-confined photocatalysts designed in porous materials for environmental uses and solar fuels, Chem. Soc. Rev. 47 (2018) 8072–8096.

[13] R. Hannes, V. Hartwig, K. Nadine, K. Susanne, W. Alexander, F. Armin, C. Jgrgen, R. Stefan, V. Ingolf, High-flux carbon molecular sieve membranes for gas separation, Angew. Chem. Int. Ed. 56 (2017) 7760–7763.

[14] M.L. Ren, J.Q. Bao, P.F. Wang, C. Wang, Y.H. Ao, Titanium phosphate nanoplates modified with AgBr@Ag nanoparticles: a novel heterostructured photocatalyst with significantly enhanced visible light responsive activity, Front. Chem. 6 (2018) 489.

[15] M.L. Tang, J. Chen, P.F. Wang, C. Wang, Y.H. Ao, Highly efficient adsorption of uranium(VI) from aqueous solution by a novel adsorbent: titanium phosphate nanotubes, Environ. Sci. Nano 5 (2018) 2304–2314.

[16] Y.D. Liu, N. Sun, S.Y. Chen, R. Yan, P. Li, Y. Qu, Y.C. Qu, L.Q. Jing, Synthesis of nano SnO2-coupled mesoporous molecular sieve titanium phosphate as a recyclable photocatalyst for efficient decomposition of 2,4-dichlorophenol, Nano Res. 11 (2018) 1612–1624.

[17] P.P. Sun, W.W. Xiong, D. Zhu, Z.H. Dong, X.P. Jin, B.B. Liu, Y. Zhang, B.H. Bao, W.F. Yao, L. Zhang, F.F. Cheng, An ultrasensitive electrochemical cytosensor for highly specific detection of HL-60 cancer cells based on metal ion functionalized titanium phosphate nanospheres, Analyst. 143 (2018) 5170–5175.

[18] y. Zhu, H. George, K. Kazuyoshi, N. Kazuki, Comprehensive studies on phosphoric acid treatment of porous titania toward titanium phosphate and pyrophosphate monoliths with pore hierarchy and a nanostructured pore surface, Inorg. Chem. Front. 5 (2018) 1397–1404.

[19] C.Y. Wang, Q.Y. Cheng, Y.J. Wang, Anion-controlled cation-exchange process: intercalating α-titanium phosphate through direct ion exchange with alkylammonium salts, Inorg. Chem. 57 (2018) 3753–3760.

[20] J.N. Zhang, Z. Ma, J. Jiao, H.F. Yin, W.F. Yan, W.H. Edward, J.H. Yu, S. Dai, Layer-by-layer grafting of titanium phosphate onto mesoporous silica SBA-15 surfaces: synthesis, characterization, and applications, Langmuir. 25 (2009) 12541–12549.

[21] X.L. Jin, C.D. Lv, X. Zhou, C.M. Zhang, Q.Q. Meng, Y. Liu, G. Chen, Molecular adsorption promotes carrier migration: key step for molecular oxygen activation of defective $Bi_4O_5I_2$, Appl Catal B-Environ. 226 (2018) 53–60.

[22] E. David, K.S. Thierry, R. Gadi, Understanding oxygen activation on metal- and nitrogen-codoped carbon catalysts, ACS Catal. 8 (2018) 8618–8629.

[23] Q. Zhang, X.X. Qin, F.P. Duan Mu, H.M. Ji, Z.R. Shen, X.P. Han, W.B. Hu, Isolated platinum atoms stabilized by amorphous tungstenic Acid: metal–support interaction for synergistic oxygen activation, Angew. Chem. Int. Ed. 57 (2018) 9351–9356.

[24] S. Mihai, M.V.B. Adrian, S. Radu, Heme Fe-SO^{2-} intermediates in sulfite reduction: contrasts with Fe-OO^{2-} species from oxygen-oxygen bond activating systems, Int. J. Quantum Chem. 118 (2018) 25697.

[25] W.J. Yang, Y.F. Zhua, F. You, L. Yan, Y.J. Ma, C.T. Lu, P.Q. Gao, Q. Hao, W.L. Li, Insights into the surface-defect dependence of molecular oxygen activation over birnessite-type MnO_2, Appl Catal B-Environ. 233 (2018) 184–193.

[26] I. Masakazu, Y. Yukihiro, Y. Noboru, S. Tetsuro, Study of metal oxide catalysts by temperature programmed desorption oxygen adsorption on various metal oxides, J. Phys. Chem. 82 (1978) (1978) 2564–2570.

[27] Y.T. Meng, W.Q. Song, H. Huang, Z. Ren, S.Y. Chen, L.S. Steven, Structure-property

[28] S.P. Rong, K.Z. Li, P.Y. Zhang, F. Liu, J.Y. Zhang, Potassium associated manganese vacancy in birnessite-type manganese dioxide for airborne formaldehyde oxidation, Catal. Sci. Technol. 8 (2018) 1799–1812.

[29] B. Liu, C.M. Li, G.Q. Zhang, X.S. Yao, S.C.C. Steven, Z. Li, Oxygen vacancy promoting dimethyl carbonate synthesis from CO_2 and methanol over Zr-doped CeO_2 nanorods, ACS Catal. 8 (2018) 10446–10456.

[30] Y. Liu, W.J. Yang, P.Y. Zhang, J.Y. Zhang, Nitric acid-treated birnessite-type MnO_2: an efficient and hydrophobic material for humid ozone decomposition, Appl. Surf. Sci. 442 (2018) 640–649.

[31] Y.F. Sun, Q.H. Liu, S. Gao, H. Cheng, F.C. Lei, Z.H. Sun, Y. Jiang, H.B. Su, S.Q. Wei, Y. Xie, Pits confined in ultrathin cerium(IV) oxide for studying catalytic centers in carbon monoxide oxidation, Nat. Commun. 4 (2013) 2899.

[32] J.L. Wang, G.K. Zhang, P.Y. Zhang, Layered birnessite-type MnO_2 with surface pits for enhanced catalytic formaldehyde oxidation activity, J. Mater. Chem. A Mater. Energy Sustain. 5 (2017) 5719–5725.

[33] T. Mylène, R. Daniela, Complete column trials for water refinement using titanium (IV) phosphate sorbents, ACS Sustainable Chem. Eng. 6 (2018) 6157–6165.

[34] G.X. Zhao, J.X. Li, L. Jiang, H.L. Dong, X.K. Wang, W.P. Hu, Synthesizing MnO_2 nanosheets from graphene oxide templates for high performance pseudosupercapacitors, Chem. Sci. 3 (2012) 433–437.

[35] P.F. Xia, B.C. Zhu, B. Cheng, J.G. Yu, J.S. Xu, 2D/2D g-C_3N_4/MnO_2 nanocomposite as a direct Z-scheme photocatalyst for enhanced photocatalytic activity, ACS Sustainable Chem. Eng. 6 (2018) 965–973.

[36] H.Q. Jiang, Y.D. Liu, S.Y. Zang, J.S. Li, H.Y. Wang, Microwave-assisted hydrothermal synthesis of Nd, N, and P tri-doped TiO_2 from $TiCl_4$ hydrolysis and synergetic mechanism for enhanced photoactivity under simulated sun light irradiation, Mat Sci Semicon Proc. 40 (2015) 822–831.

[37] H. Li, H. Shang, X.M. Cao, Z.P. Yang, Z.H. Ai, L.Z. Zhang, Oxygen vacancies mediated complete visible light NO oxidation via side-on bridging superoxide radicals, Environ. Sci. Technol. 52 (2018) 8659–8665.

[38] T. Li, G. Zhang, H.C. Lan, H.J. Liu, J.H. Qu, Enhanced photoreduction of chromium (VI) intercalated ion exchange in $BiOBr_{0.75}I_{0.25}$ layers structure by bulk charge transfer, ACS Sustainable Chem. Eng. 7 (2019) 2429–2436.

[39] X. Wang, H. Shi, H.K. Ja, S. János, Mechanism of CO_2 hydrogenation on Pd/Al_2O_3 catalysts: kinetics and transient DRIFTS-MS studies, ACS Catal. 5 (2015) 6337–6349.

[40] K.P. Deepak, B. Ayonbala, P. Kulamani, S.K. Singh, K.G. Malay, Visible light active single-crystal nanorod/needle-like α-MnO_2@RGO nanocomposites for efficient photoreduction of Cr (VI), J. Phys. Chem. C. 121 (2017) 6039–6049.

[41] A.P. Paul, D.L. Jennifer, B.M. Christopher, M.V. John, Thermal and photocatalytic reactions of methanol and acetaldehyde on Pt-modified brookite TiO_2 nanorods, ACS Catal. 8 (2018) 11834–11846.

[42] Y.K. Hyun, M.L. Hyuck, H. Graeme, CO oxidation mechanism on CeO_2-supported Au nanoparticles, J. Am. Chem. Soc. 134 (2012) 1560–1570.

[43] X.J. Wei, B. Shao, Y. Zhou, Y. Li, C.C. Jin, J.Y. Liu, W.J. Shen, Geometrical structure of the Gold–Iron(III) oxide interfacial perimeter for CO oxidation, Angew. Chem. Int. Ed. 57 (2018) 11289–11293.

[44] S. Naemeh, K. Elaheh, Novel TiO_2/graphene oxide functionalized with a cobalt complex for significant degradation of NOx and CO, RSC Adv. 5 (2015) 93706–93716.

[45] T.T. Zhang, S.T. Wang, F. Chen, Pt−Ru bimetal alloy loaded TiO_2 photocatalyst and its enhanced photocatalytic performance for CO oxidation, J. Phys. Chem. C. 120 (2016) 9732–9739.

[46] S. Naemeh, K. Elaheh, TiO2/in-situ reduced GO/functionalized with an IL-Cr complex as a ternary photocatalyst composite for efficient carbon monoxide deterioration from air, Appl Catal B-Environ. 206 (2017) 184–193.

[47] B. Florence, A. André, K. Nicolas, K. Valérie, Room temperature visible light oxidation of CO by high surface area rutile TiO2-supported metal photocatalyst, Appl Catal B-Environ. 69 (2007) 133–137.

[48] K. Elaheh, A. Soheil, In-situ functionalization of mesoporous hexagonal ZnO synthesized in task specific ionic liquid as a photocatalyst for elimination of SO_2, NOx, and CO, J. Solid State Chem. 256 (2017) 141–150.